CHAPTER IV
The modelling

The modelling involves several discrete steps before conclusions can be drawn. First, the potential of the galaxy has to be modelled and assembled from luminous and dark matter components. This includes the derivation of the stellar gravitational potential from the K-band images and, for each pre-defined disk mass fraction, a dark matter halo profile to match the observed rotation curve. The second step involves the hydrodynamic gas simulations within the combined stellar and dark matter potential. The final third step comprises the comparison of the simulated and observed gas properties, which then lead to the conclusions.

4.1. Deriving the potential from NIR observations

4.1.1. K-band Light as Tracer of the Stellar Mass

The stellar potential of a galaxy must be derived directly from its stellar mass density. To this end, it is important to understand how well the NIR surface brightness traces the stellar mass density. Stellar population and galaxy evolution modelling suggests that the overall M/L might vary by about a factor of 2, caused by the broad range of possible underlying star formation histories (see, e.g., Gavazzi, Pierini, & Boselli 1996; Cole et al. 2000; Bell & de Jong 2001). Also within a single system M/L is not entirely constant. There are two major concerns which complicate the direct translation of K-band light to mass: both dust extinction and spatial population differences could introduce local K-band mass-to-light ratio variations.

Observing at $\sim 2\,\mu$m reduces the effect of the dust extinction significantly. Since most galaxies are seen from a nearly face-on perspective, the optical depths are expected to be low, ~ 0.5 in the K-band, leading to local flux attenuations of $< 10\%$ (Rix & Rieke 1993, Rix 1995).

Population effects most likely introduce the dominant uncertainty, although also here the NIR provides a much more homogeneous estimate than optical imaging. Significant global M/L-variations may arise mainly from red supergiants; they emit most of their light in the near infrared and are fairly numerous and thus could considerably affect the total light distribution in K-band images. Supergiants evolve very rapidly and therefore are primarily found close to the spiral arms where they were born. This would tend to increase the arm-interarm contrast, leading to stronger inferred spiral perturbations in the stellar potential.

Recent studies have revealed however, that the stellar M/L correlates tightly with galaxy colors (Giraud 1998; Bell & de Jong 2001). This correlation can be used to correct for differences in the stellar M/L arising from population effects.

4.1.2. Color correction

From spiral galaxy evolution models, and assuming a universal IMF, Bell & de Jong (2001) find that stellar mass-to-light ratios correlate tightly with galaxy colors. Their models of radially resolved stellar population colors were constructed using the stellar population synthesis models of Bruzual & Charlot (2002, in preparation), and adopting a scaled Salpeter IMF (Salpeter 1955). The original Salpeter IMF was modified by globally scaling down its stellar M/L by a factor of 0.7 (see Fukugita, Hogan, & Peebles 1998) forcing it to agree with observational maximum disk M/L constraints. This global reduction in stellar M/L is essentially the same as adopting an IMF with fewer low-mass stars, as the low-mass stars contribute only to the mass, but not to the luminosity or color, of the stellar population (Bell & de Jong 2001). Derived from these models, Bell & de Jong provide color dependent correction factors, which can be used to adjust the K-band images to constant M/L.

In light of this, it is useful to stress again that the absolute M/L of a particular galaxy strongly depends on its underlying star formation history that is very difficult to assess. However, the M/L–color correlation allows the correction for relative differences in the stellar M/L, providing a mass map with some unknown value for the global M/L.

4.1.2.1. Performing the color correction

The color correction was done using the relations provided by Bell & de Jong (2001). For $(V-K)$ and $(B-K)$ colors they are:

$$\log_{10}(\mathrm{M/L}) = (-1.078 + 0.314\,(V-K)) \tag{4.1}$$

$$\log_{10}(\mathrm{M/L}) = (-0.930 + 0.206\,(B-K)) \tag{4.2}$$

The correction is done on a pixel by pixel basis for coaligned NIR and optical images. To remove the effect of noise in the images, they were convolved to a resolution of $\approx 5''$. At each point, $\mathrm{M/L}(x,y)$ was calculated according to the above equations. In a second step the M/L-map was normalized by the M/L from the global color of the galaxy, $\langle \mathrm{M/L} \rangle$, and multiplied with the K-band image.

$$\mathrm{F}(x,y)_{\mathrm{corr}} = \mathrm{F}(x,y)_K \, \frac{\mathrm{M/L}(x,y)}{\langle \mathrm{M/L} \rangle}. \tag{4.3}$$

All dust reddening effects (self absorption and galactic reddening) were ignored because the dust extinction vector nearly coincides with the color-M/L correlation of the population effects (see Figure 1d in Bell & de Jong 2001). Moreover, the typical internal extinction caused by the presence of dust at the levels expected in most galaxies is very low and on the order of 0.05 mag in the K-band (Silva et al. 1998). Still, as it has been pointed out by Bell & de Jong (2001), for optically thick dust lanes the visible light can get totally absorbed and the correction fails, if used on a pixel by pixel basis. For the

intended purposes a global mass map of the galaxies is mainly of interest. Furthermore, the moderate resolution V- and B-band images – that were even convolved to a $\approx 5''$ resolution for the correction – do not permit the discernment of thin dust lanes from regions of low surface brightness reliably. On the other hand, none of the sample galaxies exhibits prominent dust absorption features, hence one can be confident that the errors introduced from optically thick dust lanes are minor and might be ignored in a first order correction.

The optical V- and B-band images needed for the color correction were taken from the literature and from the dataset of Ph. Héraudeau (Héraudeau & Simien 1996). Table 4.1 provides a list of the optical data that was used.

Table 4.1 Sample of optical data for the color correction of the simulation sample.

Galaxy	band	brightness [mag]	resolution [$''$ FWHM]	reference
NGC 3810	B	11.30	4.4	Frei et al. 1996
NGC 3893	B	11.20	1.5	Tully et al. 1996
NGC 4254	g^*	9.86 (V)	2.4	Frei et al. 1996
NGC 5364	B	11.25	4.5	Frei et al. 1996
NGC 5676	V	11.20	2.3	Héraudeau & Simien 1996
NGC 6643	B	11.77	3.3	Héraudeau & Simien 1996

* Note: The g-filter (Thuan & Gunn 1976) has a passband that is very similar to the Johnson V-filter. Thus, the color correction given for $V-K$ can be applied to $g-K$ colors, without introducing substantial systematic errors.

The correction was performed for the galaxies for which kinematic data is available. Unfortunately for the galaxies NGC 2339 and NGC 2964 there is no useful optical image available from the literature.

4.1.2.2. Results from the color correction

The color correction was performed to obtain a better stellar mass map of a galaxy than the K-band image provides. For the sample of the 6 galaxies for which the color correction was performed the two main effects of the color correction on the galaxy and rotation curve modelling are: the change in disk scale length and the change of the non-axisymmetric force components.

The disk scale length gets shorter for all sample galaxies due to the fact that galaxy disks tend to get bluer with increasing radius (e.g., Gadotti & dos Anjos 2001). A comparison of the different scale lengths is provided in Table 4.2. The scale lengths were derived from inclination corrected images and were determined from azimuthally averaged density profiles. The disk slope was taken from a simultaneous fit of two exponentials. The effects of the color correction are displayed for NGC 5676 in Figure 4.1.

As is apparent from Table 4.2, the effect of the color correction on the disk scale length is on the order of 10 %. A shorter disk scale length is equivalent to a steeper decrease of the stellar mass with radius. The rotation curve that results from this mass distribution has a slightly shifted radius of its maximum velocity and a faster decline for large radii.

Table 4.2 Disk scale lengths for color corrected galaxies.

Galaxy	Distance	disk scale length						$\Delta R_{\rm exp}$
		optical		K'-band		color corr.		$K' \rightarrow$ c. c.
	[Mpc]	[″]	[kpc]	[″]	[kpc]	[″]	[kpc]	[%]
NGC 3810	13.5	29.2	1.91	16.3	1.07	13.9	0.91	14.7
NGC 3893	17	24.0	1.98	21.9	1.80	21.1	1.74	3.5
NGC 4254	20	43.1	4.18	36.5	3.54	31.5	3.06	13.6
NGC 5364	25	63.0	7.64	53.1	6.43	49.9	6.06	5.7
NGC 5676	33	27.7	4.43	22.4	3.59	19.5	3.12	12.9
NGC 6643	23	31.4	3.50	24.4	2.72	22.3	2.48	8.6

This fact plays a role for disk-halo decompositions for which an axisymmetric disk and halo model generally provides the basis on which to derive the rotation curves. The effect of how the color correction influences the shape of the rotation curve is shown in Figure 4.2.

Although the rotation curve does not dramatically change its shape, the correction has consequences for disk-halo decompositions. Many studies try to constrain the properties of dark halo profiles by fitting halo models on top of the stellar mass rotation curve estimates to match the galaxies' rotation curves (e.g., Verheijen 1997; Palunas & Williams 2000). The conclusions of these studies sometimes depend extremely on the accurate rotation curve shapes, i.e. the underlying mass distributions.

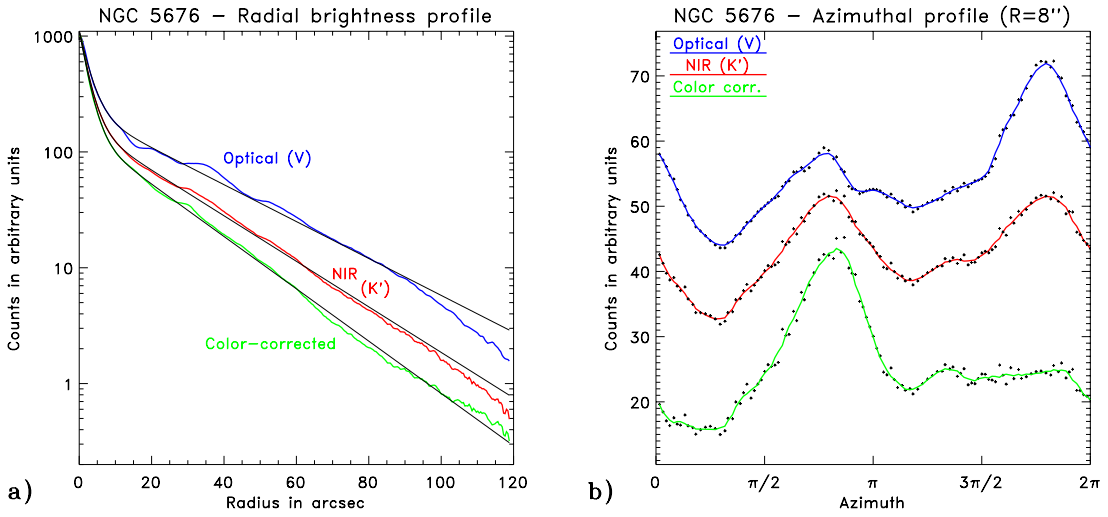

Figure 4.1 The effects of the color correction, displayed for the example of NGC 5676. **a)** shows the V-band, K-band and color corrected radial brightness profiles. Due to the outward blueing of the disk, the color corrected profile becomes steeper than both other profiles. **b)** shows how the color correction affects the local light profile. Displayed is an azimuthal cut (radius = 8″, azimuth 0 is north) through the optical, NIR and color corrected images. The two-arm profile of the galaxy is clearly visible. Features get enhanced if they are redder, or attenuated if they are bluer.

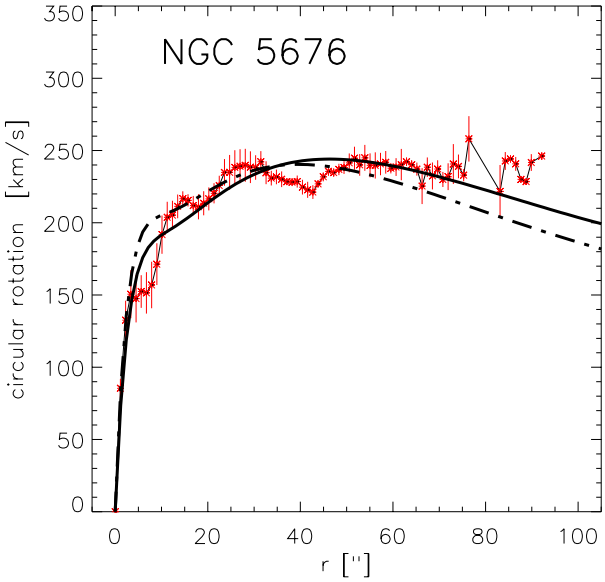

Figure 4.2 Maximal disk-only fits to the Hα rotation curve (red data points). The solid line represents the axisymmetric rotation curve taken from the K-band mass model while the dash-dotted line is the resulting rotation curve from a mass model taken from the color-corrected K-band image.

Here the color correction may help to improve the significance of the findings and might be considered. It is also expected that the color correction has an effect on the magnitude of the forces that act inside the disk. In particular the change in the radial mass distribution and the fact that the spiral arms themselves tend to be bluer, modifies the force components. In light of hydrodynamical gas modelling, where perturbations from non-axisymmetric features are studied, it is of immediate interest to quantify the change that the color correction introduces.

In this study, the force field in a galaxy gets calculated by first deriving the galaxy's gravitational potential from its surface mass distribution (as described in more detail in § 4.1.5) and by performing a numerical differentiation of the 2D potential to yield the forces. To investigate the effect of the color correction, the forces on each point in the image array were then separated into radial (F_R) and tangential (F_ϕ) components and a non-axisymmetric force fraction was defined by $F_{\rm nax} = F_\phi / F_R$. When calculating the force-field from K-band images it is found that $F_{\rm nax}$ for the sample galaxies is on the order of a few percent: The median value of $F_{\rm nax}$ for the 2D force field ranges from 2.3 % for NGC 3893 to 4.6 % for NGC 5364. Interestingly, the color correction leaves this quantity essentially unchanged. However, the change in forces on local scales is not at all constant. If $F_{\rm nax}$ is compared to $F_{\rm nax}^{\rm corr}$ and a parameter $\Delta F_{\rm nax}$ is defined by $\Delta F_{\rm nax} = |F_{\rm nax} - F_{\rm nax}^{\rm corr}|/|F_{\rm nax}|$, the median of $\Delta F_{\rm nax}$ turns out to be ~ 30 %. That means on a local scale, the color correction modifies the forces by non-negligible amounts.

4.1.3. Deprojection

Before the two dimensional gravitational potential can be calculated from the color corrected K-band image, the image needs to be deprojected to correct for the inclination with which the galaxy appears on the sky. To deproject the K-band images to face on, the IDL routine `GAL_FLAT` was applied. `GAL_FLAT` comes with the non-standard astrolib IDL package and, with the use of standard IDL routines, performs polynomial warping of the images. The deprojection of the image is realized by a geometrical transformation by bilinear interpolation between the pixels of the original image.

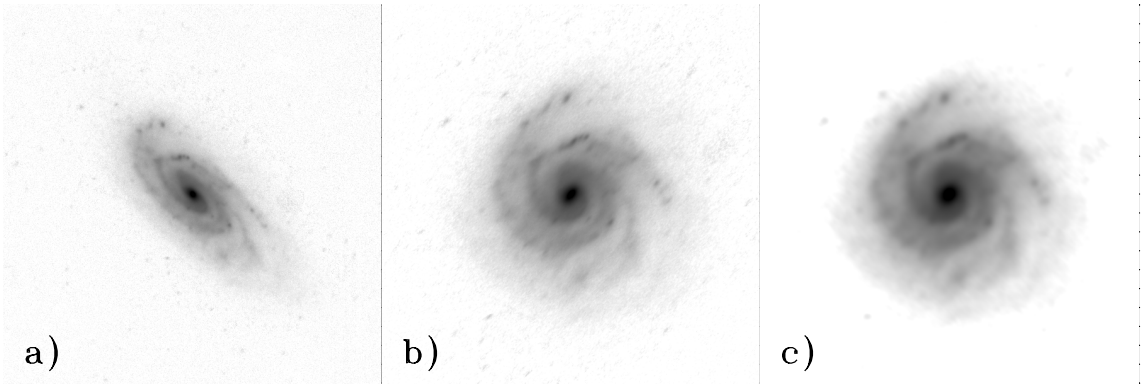

Figure 4.3 Deprojection and convolution shown for the example of NGC 5676. **a)** shows the color corrected image of the galaxy. **b)** displays the same galaxy after deprojection with a PA = 45.°8 and $i = 64°$. In panel **c)** the image was convolved with a transposed distortion function of a star in the image. Although the resolution becomes worse, point sources appear round.

Since the deprojection is in principle just a stretch of all the features in the image, for high galaxy inclinations round objects, like the nucleus of the galaxy, get exceedingly elongated. If not corrected, those asymmetric structures propagate into the potential and could introduce unwanted effects in the simulations. To correct for these distortions, the images of galaxies with inclinations of $\sim 60°$ were convolved with a transposed image of the distorted point spread function. This treatment decreases the resolution of the image, but leaves the global mass distribution virtually unchanged. The deprojection and deconvolution processes are displayed in Figure 4.3 for the exapmle of NGC 5676.

4.1.4. Cleaning the image

Some galaxies from the sample reveal quite a lot of star forming regions that are distinctly visible even in the K-band data. These regions are dominated by an overabundance of young, infrared luminous stars that exhibit a low stellar M/L. To reduce the influence of these star forming H II-regions and OB-associations, the image was filtered by means of an azimuthal Fourier decomposition. For this purpose the disk of the galaxy was modelled in Fourier space applying only the lowest, usually 8, Fourier terms. The low Fourier terms render well the overall structure of the disk, while local deviating peaks cannot be modelled. A difference map of the real galaxy and the Fourier model comprises all small scale features in the disk, such as H II-regions. After defining a certain threshold, below which the diffence map contains only noise, this clipped map can be subtracted from the

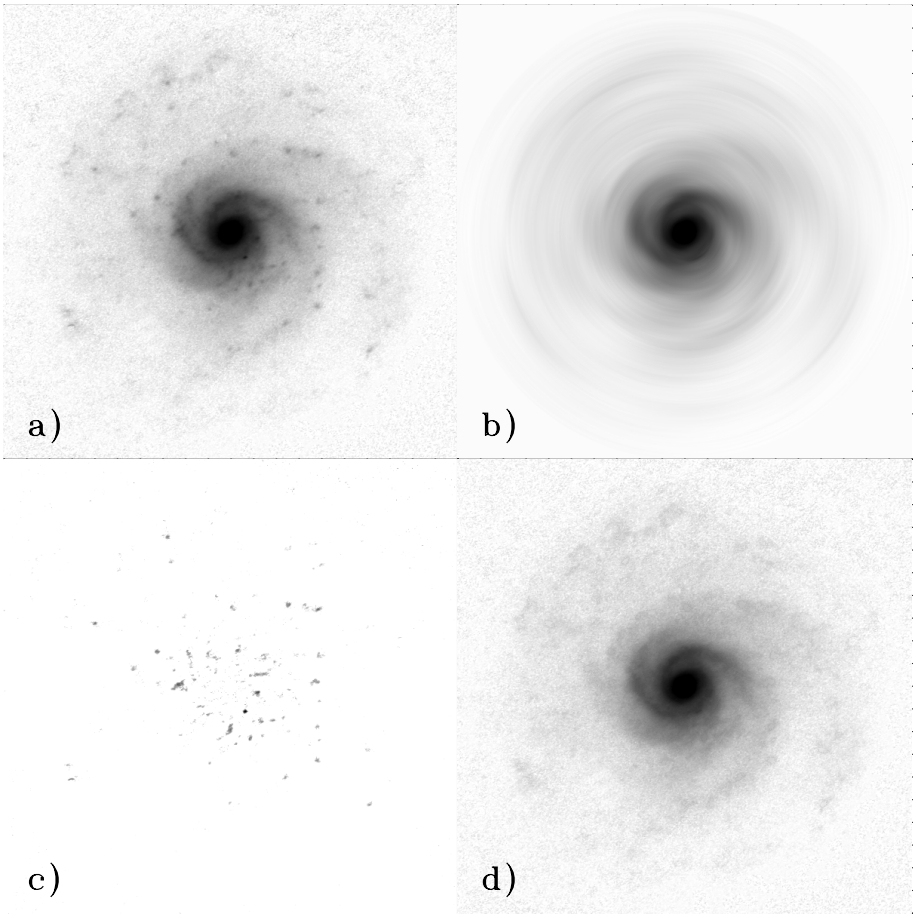

Figure 4.4 Fourier cleaning of the images shown for the example of NGC 3810. **a)** shows the color corrected, deprojected image of the galaxy. **b)** displays the Fourier model of the same galaxy applying the lowest 6 Fourier terms. In panel **c)** the clipped difference image between a) and b) is shown which is subtracted from a), yielding **d)**, the final image.

original image, cleaning it from the spiky, small scale features and leaving the smooth global spiral pattern. This process is graphically displayed in Figure 4.4. The amount of light that is removed from the K-band image depends on the number of star forming regions in the particular galaxy, but usually ranges from 1 % to 4 %. This correction does not depend significantly on the number of Fourier terms included in the fit or the choice of the threshold.

4.1.5. Calculating the stellar potential

The final image was then used to calculate a maximal disk stellar potential. This was achieved by numerical summation over the whole mass distribution of the galaxy, which is defined by multiplying the surface luminosity density L by some constant mass-to-light

ratio $\Upsilon_\star$: $\Sigma(\mathbf{r}) = \Upsilon_\star L(\mathbf{r})$. $L(\mathbf{r})$ comes from the processed K'-band images.

$$\Phi_\star(\mathbf{r}_i) = -G \sum_{j \neq i} \frac{\Upsilon_\star L(\mathbf{r}_j)}{|\mathbf{r}_i - \mathbf{r}_j|} \tag{4.4}$$

with:

$$|\mathbf{r}_i - \mathbf{r}_j| = \sqrt{\Delta \mathrm{x}^2 + \Delta \mathrm{y}^2 + \epsilon^2}. \tag{4.5}$$

The indices i and j denote different radius vectors, specifying here the pixels of the image array. Outside the detector array, the surface mass density is assumed to be zero. The factor ϵ in Equation (4.5) accounts for the finite thickness of galactic disks following Gnedin, Goodman & Frei (1995). This softening factor was chosen to be compatible with a vertical exponential density scale height of $h_z = 400\,\mathrm{pc}$, independent of radius. This assumption most probably holds for late type spirals, whose central spheroids, extend only to about a disk scale length into the disk. Additionally, small bulges may not be spherical and thus might be well described by the constant scale height of 400 pc assumed for most of the simulations. Moreover, the derived potential does not depend significantly on the choice of h_z. Varying h_z by 10 % leads to relative changes of the resulting forces by $\sim 5.1 \times 10^{-3}$ on average. An explicit disk-bulge decomposition was performed only for the most massive stellar disk models and the softening factor for the bulge was increased substantially to about 800 pc. This was necessary to achieve a better fit at the very inner part of the observed rotation curves.

Additionally a potential $\Phi_{\star,\mathrm{ax}}$ from an equivalent *axisymmetric* density distribution fitted to the galaxy's (corrected) K-band luminosity profile was calculated. This axisymmetric model potential will be used later for initializing the hydrodynamic simulations, which are set up in an axisymmetric potential. Furthermore, the modelled rotation curves that were used to scale the potentials by comparison with the observed rotation curves were calculated from the axisymmetric disk model. The model rotation curves got evaluated numerically from the stellar potentials by

$$v^2_{\star,\mathrm{ax}}(R) = R \left. \frac{d\Phi_{\star,\mathrm{ax}}(r)}{dr} \right|_R . \tag{4.6}$$

When inserting the physical dimensions for L, $\mathbf{r}$ and $\Phi_\star$ into equation (4.4) the value for $\Upsilon_\star$ can be derived for any light distribution $L(\mathbf{r})$, e.g., K' or the color corrected density, by scaling the potential such that the derived rotation curve matches the observed one. Later, when combining stellar and dark halo potentials, fractions $\mathrm{f_d}$ of this stellar 'maximum disk' fit were taken, to explore various luminous-to-dark matter ratios.

4.1.6. Determining the halo parameters

For the present analysis the radial density profile of a pseudo-isothermal sphere is used as the dark matter component in the model. Its radial density profile, characterized by a core of radius R_c and a central density ρ_c, is given by:

$$\rho(R) = \rho_c \left[1 + \left(\frac{R}{R_c} \right)^2 \right]^{-1} . \tag{4.7}$$

The corresponding rotation curve is

$$v^2_{\mathrm{halo}}(R) = v^2_\infty \left[1 - \frac{R_c}{R} \arctan\left(\frac{R}{R_c} \right) \right] \tag{4.8}$$

(Kent 1986) and the potential is

$$\Phi_{\rm halo}(R) = \int_0^R \frac{v^2_{\rm halo}(r)}{r} dr, \tag{4.9}$$

which is realized by numerical integration over the velocity profile. The asymptotic circular velocity in this (infinite mass) halo v_∞ is related to the two other free parameters R_c and ρ_c by

$$v_\infty = \sqrt{4\pi G \rho_c R_c^2}. \tag{4.10}$$

Thus, v_∞ and R_c uniquely specify all properties of the halo. For any potential with an underlying mass fraction $\mathrm{f_d}$ of the maximal stellar mass contribution it is possible to obtain the halo parameters from the best fit of the *combined* stellar and halo rotation curve to the observed kinematics. The quality of the fit was determined from a least squares analysis in the reasonable parameter range of v_∞ and R_c.

4.1.7. Assembling the final potential

In the final potential the disk and halo components were combined in the following way:

$$\Phi_{\rm tot}(\boldsymbol{R}|\mathrm{f_d}) = \mathrm{f_d}\ \Phi_\star(\boldsymbol{R}) + \Phi_{\rm halo}(\boldsymbol{R}|\mathrm{f_d}) \tag{4.11}$$

with $\mathrm{f_d}$ ranging from 0 to 1, and $\Phi_\star$ denoting the stellar potential with maximal stellar mass-to-light ratio. The contributions to the circular velocity add quadratically:

$$v^2_{\rm tot}(\boldsymbol{R}, \mathrm{f_d}) = \mathrm{f_d}\ v^2_\star(\boldsymbol{R}) + v^2_{\rm halo}(\boldsymbol{R}, \mathrm{f_d}). \tag{4.12}$$

For every $\mathrm{f_d}$ it was possible to find a dark matter profile, which complements the luminous matter rotation curve to match the measured rotation curve with closely comparable quality. Figure 4.5 shows this for the example of NGC 4254.

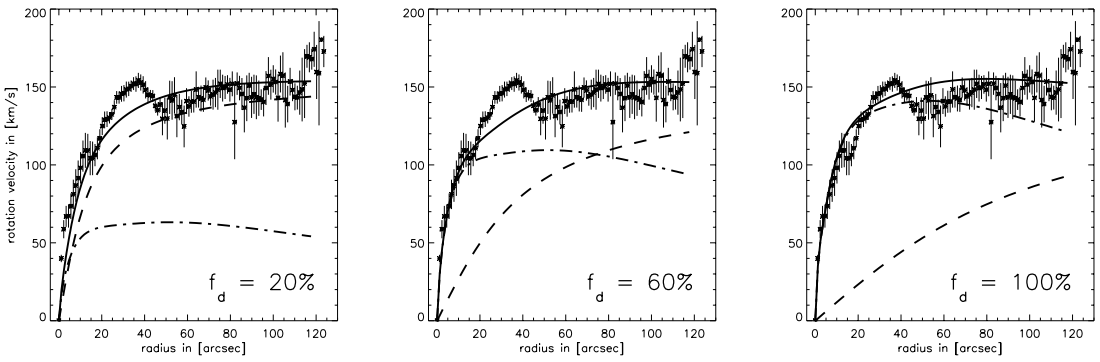

Figure 4.5 Different decompositions of the total gravitational potential into stellar and dark halo components, illustrated for the example of NGC 4254. The measured rotation curve (*data points with error bars*) – an average of six single rotation curves closest to the major axis – is well fit by all decompositions (*solid line*). Displayed are three cases for the contribution of the stellar disk $\mathrm{f_d} = 20\,\%$, 60 % and 100 % (*dash-dotted line*). The halo contribution (*dashed line*) was adjusted to yield a good fit to the measurements in combination with the pre-selected stellar contribution.

4.2. Hydrodynamic gas simulations

Hydrodynamic modelling of a gas flow could be based on either a macroscopic or microscopic description of the gas processes. In the macroscopic case the formalism is based on the Euler and Navier-Stokes equations, while the microscopic description relies on the (collisional) Boltzmann equation. A large fraction of hydrodynamic codes in the literature are based on solving the Euler equations, which do not include viscosity and heat conductivity in the gas description. To simulate realistic processes, additional terms, adapted to the Navier-Stokes problem must be included. These schemes work with varying success in realistic applications and often fail in extreme situations like strong shocks and rarefied gas dynamics. Alternatively, schemes may be based on the gas kinetic theory, evolving the particle distribution function with the Boltzmann equation. While schemes based on the collisionless Boltzmann equation are robust, the inclusion of the highly complex collision term into the hydrodynamic simulation scheme promises more accurate results. The hydrodynamic code, employed to model the gas flow in the sample of galaxies for this thesis is based on gas kinetic theory. It makes use of an approximation to the collisional Boltzmann equation, namely the Bhatnagar-Gross-Krook (BGK) scheme. The following sections provide a quick overview of the principles behind this approximation and the application of the numerical code to the astrophysical problem of galactic gas flows.

4.2.1. The BGK scheme

All macroscopically observed quantities characterizing a gas flow, such as mass, momentum and energy densities, rely on the microscopic behavior of the gas which can be described by the gas kinetic theory. For a numerical description of gas processes, it is possible to employ a scheme that is likewise based on the gas kinetic theory and its fundamental quantity, the particle distribution function $f(x_i, p_i, t)$. f gives the number density of particles in a six-dimensional phase space at a time t. The time evolution of the gas distribution function f is given by the collisional Boltzmann equation:

$$\frac{\partial f}{\partial t} + p_i \frac{\partial f}{\partial x_i} + a_i \frac{\partial f}{\partial p_i} = Q(f, f) \tag{4.13}$$

where a_i is the external force term acting on the particle in the i-th direction, and $Q(f, f)$ is the collision operator. For realistic gas processes, the highly non-linear and non-local collision operator is very complicated. However, for small deviations from thermodynamic equilibrium the collision operator can be substituted by a much simpler collision term, introduced by Bhatnagar, Gross & Krook (1954): $g - f/\tau$. The BGK term describes the relaxation of a non-equilibrium velocity distribution function f towards the local equilibrium state g, described by the Maxwell-Boltzmann distribution function. τ is defined as the collision time. It is the timescale on which f evolves to g. Assuming τ is the same for all particles regardless of their velocities, the collision term in the Boltzmann equation (without external forcing) becomes:

$$\frac{\partial f}{\partial t} + p_i \frac{\partial f}{\partial x_i} = \frac{g - f}{\tau}. \tag{4.14}$$

The underlying assumption in the BGK scheme is that there exists a collision process that transforms the particles from f to g, while conserving the total mass, momentum and

energy. Since the relaxation towards the equilibrium state is an irreversible, dissipative process it is accompanied with an increase in entropy. By evolving f through an equation which accounts for particle collisions, the fundamental mechanism for generating dissipation in the gas, the BGK scheme naturally renders the dissipative and viscous character of the gas and, at the same time, BGK satisfies the entropy condition. Moreover, due to its gas kinetic derivation, the BGK method satisfies the macroscopic Navier-Stokes and (inviscid) Euler solutions directly in smooth regions. A good review on the BGK approximation and its implications has been provided by Xu (1998).

4.2.2. The code

The code that is used for running the hydrodynamic simulations for this thesis is based on the BGK scheme. Details of its design, technical realization and capabilities can be found in Prendergast & Xu 1993; Slyz 1998; Slyz & Prendergast 1999). It is an Eulerian, grid-based hydrodynamics code that solves for the gas particle distribution function f and computes the physical quantities, like gas density, pressure and gas fluxes from the velocity moments of f. According to equation 4.14 a solution for f is a solution to the ordinary differential equation $\frac{\delta f}{\delta t} + \frac{f}{\tau} = \frac{g}{\tau}$, where $\frac{\delta}{\delta t}$ is the total time derivative along a particle trajectory in phase space. The differential equation is solved, obeying a set of boundary conditions, requiring that during particle collisions, mass, momentum and energy are conserved, i.e. the equivalence of the moments of f and g. The mean time between collisions, τ, is calculated locally for each cell from thermodynamic quantities at the cell interfaces. The code makes use of the fact, that local fluxes, and therefore a solution of f, is only required at cell interfaces of the underlying grid and for discrete time steps, therefore a solution for f can be numerically approximated. Clumpy structure of the gas on scales less than the grid size remains unresolved.

4.2.2.1. The collision time τ and its approximations

One of the basic parameters for the gas simulations is the collision time τ that needs to be locally computed during the runs according to the actual conditions. For the flux computation, the BGK scheme solves the BGK equation for f in the neighborhood of the boundary of each computational cell and for a short time, given by the usual Courant-Friedrichs-Lewy (CFL) condition, using a locally computed value for the collision time τ.

In practice the collision time, τ is composed of two terms: the first term corresponds to a real viscosity that is active everywhere including in smooth flow regions, whereas the second term is there for numerical purposes, namely to resolve discontinuities in the flow. For Euler calculations, which are used in the present case, the first term can be taken as $\mathcal{C}_1 \Delta \mathrm{t}_{\mathrm{CFL}}$, where a reasonable value for $\mathcal{C}_1$ is 0.01, i.e. assume 100 collisions per CFL timestep. Alternatively, for Navier-Stokes calculations, this term can be derived from gas kinetic theory which links the collision time to the gas density ρ and temperature T.

For problems in which the gas flow has discontinuities, the collision time τ serves an additional purpose. If the grid is not fine enough to resolve a discontinuity, then artificial dissipation must be added to broaden the discontinuity so that it is at least one grid cell thick. Because viscosity and heat conductivity are proportional to τ, the BGK scheme broadens shocks by enlarging τ at the location of the discontinuities. The expression for the collision time in the BGK scheme therefore contains a second term which is chosen in

such a way that shocks in the flow span at least one grid cell. This second term tunes the amount of artificial dissipation in the scheme. The notable difference between how the BGK scheme inputs artificial dissipation and how other schemes input artificial dissipation is that the BGK scheme puts it in exactly as if it were real dissipation corresponding to the numerically necessary value for τ. It should be emphasized that neither the artificial dissipation nor the physical dissipation enter the scheme as a predefined source term. When the second term in the collision time dominates, the order of the scheme is reduced and the true distribution function f is determined more by the initial distribution function f_0 than by the integral over g.

As far as approximations go when solving for f at a cell wall in the BGK scheme, it is assumed that all particles in that local region have the same particle collision time τ regardless of their velocity. As a result of this, the BGK scheme only gives Navier Stokes solutions with a fixed Prandtl number of 1. For this project that is acceptable because one is interested in getting accurate Euler solutions as opposed to Navier-Stokes ones. Another important point regarding τ is that it is a way to add dissipation into the flow homogeneously in all directions.

In summary, in the BGK scheme, the collision time τ ranges from a physically reasonable value, either computed locally on the basis of gas kinetic theory for Navier-Stokes problems, or assumed to be about 100th of the updating timestep for Euler problems, to a numerically necessary value (where $\tau \approx \Delta t_{\mathrm{CFL}}$, the CFL timestep). By this variation of the collision time throughout a hydrodynamical computation, the BGK scheme can describe a numerical fluid in both smooth and discontinuous regions.

4.2.2.2. Application to galactic gas simulations

The simulations of gas flows in galactic disks are challenging because cold gas in galactic disks rotates with such high Mach numbers that if the flow is diverted from a circular orbit by non-axisymmetric forces, the consequence is etched in the gas in patterns of shocks and rarefied regions. The BGK-code is well suited for these simulations because as verified by extensive tests on standard 1D and 2D test cases of discontinuous non-equilibrium flow (for a review, see Xu 1998), at shocks and contact discontinuities BGK behaves as well as the best high resolution codes and it gives better results at rarefaction waves because it naturally satisfies the entropy condition. However, treating rarefied gas dynamics with a hydrodynamics code will always be dissatisfactory because by definition, hydro assumes that there are an infinite number of collisions between the gas particles in a timestep or that the collision time is on the order of the updating timestep. In the regime where $\rho \to 0$ the collisional Boltzmann equation is inappropriate. The governing dynamical equation should be the collisionless Boltzmann equation in which case one is required to save much more information than the lower order moments of f. In BGK, when $\rho \to 0$, and hence $\tau \to \infty$, the distribution function f from which fluxes are computed goes to the initial distribution function f_0. The fact that BGK is not wired to exclusively solve the Euler or Navier-Stokes equations but that it can be applied to a broader range of τ's means that it is generally more robust for rarefaction waves than hydrodynamical codes based directly on the Euler or Navier-Stokes equations.

BGK has been used to solve Navier-Stokes problems in smooth flow regions both with (Slyz et al. 2002) and without (Xu & Prendergast 1994) gravity, and it has been tested

for its long-term stability and convergence to the equilibrium solution in a fixed external gravitational field (Slyz & Prendergast 1999). One additional reason for carrying out the disk simulations with this code, is its low diffusivity, a property that is critical not only to capture the shocks that form when the gas circulates in the non-axisymmetric potential, but also to properly model the loss of angular momentum and hence the resulting radial inflow of the gas due to the strong shear in the underlying differentially rotating disk. Slyz et al. (2002) showed that if an isothermal gas is initialized to be in centrifugal equilibrium within a purely axisymmetric galactic potential, simulation with the BGK scheme produces the steady-state Navier-Stokes solution to a high degree of accuracy. The success of BGK in giving viscous radial flows on the order of 1 $\mathrm{km\,s^{-1}}$ in a disk rotating differentially at 220 $\mathrm{km\,s^{-1}}$ is remarkable. It is a technical success which insures that when studying the kinematics of the gas in a galactic disk with BGK, with a decent grid resolution, one can worry less about artificial dissipation.

At its present state, the code does not allow the consideration of additional forces arising from the gas self-gravity. However, given that the gas surface mass density of the modelled galaxies is much lower than the density of the stellar disk and halo, it seems safe to assume that neglecting the gas self-gravity leads only to second order effects.

4.2.3. Boundary conditions

Since the computations were done on a Cartesian grid, the center of the disk (r = 0) is not a singular point, and therefore does not require special treatment via an inner boundary condition. Instead gas flow is computed through this point as it is computed through any other point on the grid.

An outer boundary condition is, on the other hand, unavoidable. Outside of a radius of R_{disk} two "rings" of ghost cells were kept, each "ring" being one cell thick. Beyond these ghost cells the evolution of the gas is not followed. Hence, effectively a circular grid is carved out of the square Cartesian grid. At the end of each updating timestep the values of the hydrodynamic quantities (mass, momentum and energy) were updated in the ghost cells by performing a bilinear interpolation to the cells in the vicinity of that ghost cell. To be more specific, for each ghost cell in the inner ring, for example, the coordinates of the intersection of the line extending radially from the center of the disk to the ghost cell with the circle bounding the true flow region of the grid get computed. After fitting a surface to the hydrodynamic quantities in the four cells surrounding this intersection (some of them might be other ghost cells) the ghost cell gets assigned the value that the fitted surface has at the intersection. Filling up the ghost cells via constant radial extrapolation that varies azimuthally around the disk, enables a better handling of situations in which there is a significant non-axisymmetry near the outer boundaries. The potential of NGC 4254 for example is quite non-axisymmetric near the upper boundaries thereby requiring an outer boundary condition which can take into account the possibility that the flow in the outer regions of the disk may also be non-axisymmetric.

As a further detail, it must be pointed out that this procedure for computing the outer boundary conditions is applied directly to the mass densities, however, for the velocities, additional steps were taken. The Cartesian velocity components were converted back to the non-rotating frame, then the radial and tangential components of the velocity were

constructed from the Cartesian components, and the bilinear interpolation and radial extrapolation procedure was finally performed on these components. By performing the interpolation and extrapolation on the radial and tangential components in the non-rotating frame, the boundary conditions were first set for quantities that are easier to interpolate and extrapolate: namely the tangential velocity which is nearly flat (constant in x and y) and the radial velocity which is nearly zero in the disk's outer regions in the non-rotating frame.

The outer boundaries allow gas flow across them. For different runs, mass loss/gain due to gas flow across them ranges after about 1 $t_{\rm dyn}$ from $\approx 2\%$ for runs performed in the non-corotating frame or slowly corotating frames, to at most $\approx 15\,\%$ for the fastest corotating frames that were simulated.

4.2.4. Performing the simulations

The gas density profiles were initialized to be exponential with a scale length which is a third of the radius of the observed disk. Upon estimating the total mass of the galaxy from the observed rotation curves, the mass of the gaseous disk was set to be 5% of this total mass so that the gas is moving in a potential produced by a mass much greater than the gaseous component, thereby justifying the neglect of the gas's self-gravity.

Given that the difficult question of how the spiral formed is beyond reach in these simulations, the focus is not to look for time-dependent solutions, but instead for steady or quasi-steady flow in NGC 4254's fixed external gravitational potential. The gas must therefore satisfy:

$$\boldsymbol{u} \cdot \nabla \boldsymbol{u} + 2\Omega_{\rm p} \times \boldsymbol{u} = -\nabla p/\rho \pm \nabla\Phi \tag{4.15}$$

$$\nabla \cdot (\rho \boldsymbol{u}) = 0 \tag{4.16}$$

where Φ is the potential of the *combined* centrifugal and gravitational forces. This system of equations must be completed by an equation of state and this introduces another parameter in the modelling, the gas sound speed. Since an effective equation of state is unknown for the interstellar medium (ISM), the simplest thing to do is to assume an isothermal equation of state so that $p = K\rho$. Here K is a constant. It is equal to ${c_s}^2/\gamma$ where γ is the ratio of specific heats of the gas, and $c_s = \sqrt{\gamma \mathsf{R}T/\mathsf{M}}$ is its sound speed. $\mathsf{R} = 8.314\ \mathrm{J\,mol^{-1}\,K^{-1}}$ is the gas constant; T is the ideal gas temperature in K; M is the molecular weight of the gas in $\mathrm{kg\,mol^{-1}}$. The isothermal equation of state implies a one-component model of the ISM. To compensate for a multiphase ISM, the behavior of the gas flow was studied with changing sound speed for the example of NGC 4254. The validity of the conclusions with a one-component ISM, depend mainly on the similarity between the large-scale dynamics of a one-phase model and a multi-phase model.

The simulations were performed on an evenly spaced Cartesian grid. The resolution per grid element was chosen to measure about 100 pc in real units for each galaxy. For NGC 4254 the additional cases for grid cell sizes of ≈ 50 and ≈ 200 pc were explored.

The simulations were started with the gas flowing on circular orbits in inviscid centrifugal equilibrium with respect to the axisymmetric gravitational potential which best fits the observed rotation curves. The non-axisymmetric perturbations (whose strength is determined by the disk fraction, $\mathrm{f_d}$, of the model), are then turned on gradually. As Sorensen

& Matsuda (1982) describe, if the potential is turned on too rapidly, material arms are produced in the gas simulations. These will be wound up by the differential rotation of the disk, and will eventually disappear by winding. A slow turn-on of the potential avoids or at least minimizes this transient. The criteria for the time in which the full potential was turned on, ($t_{\rm FP}$), was adjusted according to the sound crossing time ($t_{\rm s}$) across the diagonal of a grid cell. For the standard simulations $t_{\rm FP} = 40\ t_{\rm s}$ was chosen. Since the sound crossing time depends on the length of the grid cell, and for comparison's sake the total running time of each simulation should be similar, $t_{\rm FP}$ was scaled with $t_{\rm s}$ for the additional high- and low-resolution runs. After the full potential was turned on, the runs were set up to continue for another one to two dynamical times.

The computations were performed in the non-inertial coordinate system rotating with the pattern speed $\Omega_{\rm p}$. This is another parameter of the simulation which turns out to play a powerful role in shaping the morphology of the gas distribution. The direction of the coordinate system rotation depends on the sense in which the arms of a galaxy wind. It is chosen such that, inside corotation, the gas enters the spiral arms from the concave side.

The bulk part of the simulations were done using the SGI Origin 2000 located at the Rechenzentrum Garching and which is dedicated to the Theory group of MPI für Astronomie in Heidelberg. The Origin 2000 hardware consists of 16 processors MIPS R10000 operating at 195 MHz with 8 GB main memory available. The code has capabilities to run in parallelized mode and simulation scripts were set up to run on 4 processors each. One single simulation requires about 2 hours of CPU time, depending on the number of simulated timesteps. The code is also able to run on SUN workstations.

4.3. Comparing observations and simulations

To draw conclusions from the modelling of the analyzed galaxies, the results from the simulations, namely the gas density distribution and the gas velocity field, must be compared to the observations. This Section describes the procedures that were applied to estimate or quantify how well one simulation reproduces the real conditions in a particular galaxy.

4.3.1. The gas density

The gas density output of the simulations can be used to find the pattern speed of the galaxies. For this purpose, the modelled gas density was overlaid in contours onto a real image of the galaxy. The real image, which was usually the K'-image, was displayed such that the arm structure appeared enhanced on the image. This was achieved by either subtracting an azimuthally averaged disk model from the galaxy and plotting the residual non-axisymmetric structure, or by the unsharp masking technique. The unsharp mask was created by convolving the image with a two dimensional Gaussian with a FWHM of 28 image pixels. Plotting the difference of the mask and the original yields an image emphasizing the non-axisymmetric spiral structure.

The actual comparison and determination of the best fitting model was done by eye. This might appear to be a very qualitative or biased approach. However, it is one of the eye's most powerful attributes to recognize patterns and similar structures. And since the agreement of spiral features is of a two dimensional, global nature, the eye can distinguish with

high precision between a good fit and a less good one. Eventually, since the density profiles of a gaseous shock and that of a stellar spiral arm are considerably different, any kind of quantitative least squares comparison would be very difficult to interpret. Furthermore, in most cases the winding of the spiral pattern in the simulations evolves monotonically from tight to more open structures with increasing corotation radius, which allows the unambiguous identification of the range for the best matching pattern.

Even when determining the match by eye, there are some criteria according to which to pick one particular model. In general, gas shocks appear where the streaming gas encounters the spiral pattern. Inside corotation this is at the inward facing side of the spirals, if trailing arms are assumed, because there the gas circular velocity is larger than the pattern speed. Another criterion is the location of star forming H II regions along the arms. This is a characteristic of the density wave. The shocked gas triggers star formation along the spiral arms directly downstream from where the gas is compressed the most (Schweizer 1976, Beckman & Cepa 1990). Thus, a good matching morphology would place the gas density shocks at locations, where the most star forming regions come to lie in the spiral arms.

4.3.2. The gas velocity

The observations cover the gas velocity field only along the slit positions where the spectrograph was placed across the disk. Thus, the comparison was done along these slits. To correctly compare the simulated gas velocities to the observed data, the modelled velocity field needs to be projected according to the real orientation of the galaxy. From the projected velocity field, the line-of-sight component of the velocities must be obtained along the slit positions taken with the spectrograph. For this procedure the Cartesian velocity components were transformed into velocity components parallel and orthogonal to the galaxy's major axis. The simulations yield truly two dimensional velocity fields and the component parallel to the major axis does not contribute to the line-of-sight velocity as it reflects only tangential motion. The orthogonal velocity component is multiplied by the sine of the inclination of the galactic disk, to account for the line-of-sight fraction of the velocities.

The velocities are read along slits which correspond to the slit positions taken with the spectrograph. The angular width of the grid cells of the simulation ($1\farcs19$) is comparable to the slit width of the spectrograph that was used ($1\farcs5$), which was also the average seeing conditions. The angles between the spectrograph slit orientations that were taken from the projected galaxy on the sky, must be translated to angles in the plane of the galaxy to actually compare the same parts of the velocity fields. This translation makes use of the following relationship:

$$\tan(\varphi_{\rm int} - {\rm PA}) \cdot \cos(i) = \tan(\varphi_{\rm app} - {\rm PA}) \tag{4.17}$$

where $\varphi_{\rm app}$ is the apparent angle of the spectrograph slit across the galaxy on the sky and $\varphi_{\rm int}$ is the corresponding intrinsic angle within the plane of the galaxy. PA is the position angle of the galaxy's major axis on the sky. All angles are in degrees measured eastward from north. See Figure 4.6 for a graphic representation of the relevant angles and orientations. Solving for $\varphi_{\rm int}$ gives:

$$\varphi_{\rm int} = \varphi_{\rm diff} + {\rm PA} \tag{4.18}$$

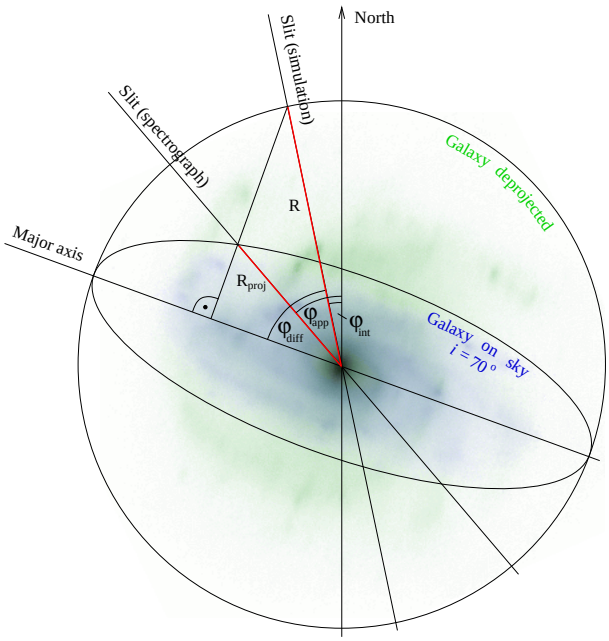

Figure 4.6 Schematic representation of the important elements of the deprojection process.

with φ_{diff} being the angle between φ_{int} and the major axis:

$$\varphi_{\mathrm{diff}} = \arctan\left(\frac{\tan(\varphi_{\mathrm{app}} - \mathrm{PA})}{\cos(i)}\right). \tag{4.19}$$

The foreshortening of the radial proportions due to projection in the direction of the minor axis is determined by

$$R_{\mathrm{proj}} = R \cdot \sqrt{\cos^2(\varphi_{\mathrm{diff}}) + (\sin(\varphi_{\mathrm{diff}}) \cdot \cos(i))^2}. \tag{4.20}$$

Finally the detector pixel sizes of the TWIN, where the observed velocities come from, and Omega Prime camera, whose pixel scale is the reference grid for the simulations, must be adjusted to perfectly align with each other.

4.3.2.1. Evaluation of the comparison

In order to quantify the degree of agreement between the observed and simulated velocity fields a least squares comparison along the spectrograph slit position was performed:

$$\chi^2 = \sum_{\text{all slits}} \sum_{\text{all r}_\mathrm{i}} \left[\frac{v(\mathrm{slit_i}, \mathrm{r_i})_{\mathrm{sim}} - v(\mathrm{slit_i}, \mathrm{r_i})_{\mathrm{obs}}}{\sigma(\mathrm{slit_i}, \mathrm{r_i})_{\mathrm{obs}} + \sigma_{\mathrm{sys}}}\right]^2 \tag{4.21}$$

where $v(\mathrm{slit_i}, \mathrm{r_i})_{\mathrm{sim}}$ and $v(\mathrm{slit_i}, \mathrm{r_i})_{\mathrm{obs}}$ are the simulated and the observed velocities respectively. $\sigma(\mathrm{slit_i}, \mathrm{r_i})_{\mathrm{obs}}$ is the error that was attributed to the measured velocities (see Section 3.3.2). Additionally, a systematic error σ_{sys} was added to all measured data points, in order to consider uncertainties that are not accounted for, like asymmetries in the Hα-line

profiles, errors in the zero-point determination of the rotation curves or eventual mismatch between the positions of the observed slit and the artificial slit across the simulated velocity field. For all galaxies a systematic error of $9.5\,\mathrm{km\,s^{-1}}$ was added to each measured data point for the χ^2-analysis. Furthermore, since the χ^2/N is very sensitive to single outliers (they add in quadratically), in ambiguous cases the median of the sum in equation (4.21) was considered too.

However, as it became evident during the process of the analysis, on small scales the simulations fail to reproduce all structures in the observed rotation curves. This effect comes from the systematic approach of the study and originates from the fact that in the modelling only the gravitationally induced gas kinematics can be reproduced. All other local gas dynamic processes, like stellar winds in the vicinity of star forming regions or supernova remnants, are left unaccounted for. Also the two dimensional nature of the simulations introduces systematic errors. These effects will be discussed in more details in the following chapters. In light of this, a global least squares comparison, including all observed data points might not be the right approach to evaluate the best match. If the amount of kinematic wiggles induced by gravity and the amount caused by other processes roughly commensurate, the global least squares comparison will systematically favor the models that exhibit the least non-axisymmetric structures to which the axisymmetric gravitational potential of the galaxy was tuned to fit, i.e. light disks.

All attempts to constrain non-gravitational wiggles from the observations turned out to yield unsatisfying results. Hα line profiles or intensities emerged as a rather inconclusive basis to separate gravitational from non-gravitational gas kinematic features. High resolution Hα maps were not available to identify gas shells or supernova bubbles. On the other hand, the hydrodynamic simulations can be used in a rather robust statistical approach to find the locations along the spectrograph slits, where the velocity fields exhibit an essentially undisturbed gravitational response to the underlying potential.

By using the simulations for the best matching pattern speed the gravitation dominated regions can be determined by selecting those parts of the rotation where the individual terms of the least squares analysis (equation 4.21) do not exceed a predefined treshold. To do this coherently, the selection process involves the models for all disk mass fractions f_d. As a criterion for an observed data point to enter the final subset for comparison, it must have been flagged at least by two f_d models as "gravity wiggle". The treshold was chosen to exclude roughly half of the total data points.

This method provides a rather unbiased approach to exclude non-gravitationally induced gas shocks because it utilizes the information from the simulations and does not preselect for a certain mass model. The final evaluation of the fit quality between the observations and simulation results for the different galaxy mass models is then performed by restricting the least squares analysis to the data points from the observations that most likely render gravitationally induced gas kinematic features.

The above described selection method was not applied to NGC 4254 because it was developed only after the results for this galaxy were published. However, applying this method to NGC 4254 does not change the conclusions derived in the paper.